Article

Analysis of VLF Electromagnetic Scattering in Lower Anisotropic Ionosphere Based on Transfer Matrix

Lin Zhao [1,*,†], Zhiting Zhan [1,2,†], Zhigang Zhang [1,†] and Huiting Feng [1,*]

1 Department of Communication Engineering, Naval University of Engineering, Wuhan 430033, China; m23285403@nue.edu.cn (Z.Z.); 0909031067@nue.edu.cn (Z.Z.)
2 Unit 91497, The People's Liberation Army, Ningbo 315100, China
* Correspondence: 0909031064@nue.edu.cn (L.Z.); 1920191204@nue.edu.cn (H.F.)
† These authors contributed equally to this work.

Abstract: Very-low-frequency (VLF) electromagnetic waves (3–30 kHz) are stable and attenuated, suitable for various applications in submarine communication and earthquake prediction. Very-low-frequency electromagnetic waves usually propagate in atmospheric waveguides formed between the anisotropic ionosphere at low to medium heights and the earth. However, the electromagnetic parameters of the anisotropic ionosphere at low to medium heights are very complex, making it difficult to accurately calculate and analyze the scattering characteristics of very-low-frequency electromagnetic waves. This article divides the mid to low altitude anisotropic ionosphere into fine layers, and establishes a more accurate transmission model for ultra-low-frequency electromagnetic waves in the layered structure of ionization layers by deriving the anisotropy/transmission matrix of each layer. In the comparative verification, we calculated the field strength of 17 kHz VLF electromagnetic waves within a transmission distance range of 500–1600 km based on the proposed method and compared it with statistical data collected from actual communication experiments and theoretical calculation results based on traditional ITU-R P.372-11. The results show that compared with the theoretical results based on ITU-R P.372-11, the method proposed in this paper fully considers the vertical height non-uniformity of the ionosphere, and its calculated results are more consistent with actual measurement data, with higher accuracy. Our work provides excellent guidance for the development of precise models for the propagation and prediction of extremely low-frequency electromagnetic waves, as well as a good idea for the accurate calculation of VLF electromagnetic scattering within 500–1500 km.

Keywords: VLF; ionospheric model; transfer matrix method

1. Introduction

Very-low-frequency (VLF) radio waves (3 kHz–30 kHz) are widely used in ultra-long-range navigation [1], communication [2], and earthquake prediction [3]. The American Omega [4] and Russian Alpha [1] systems are the most typical very-low-frequency navigation systems [5]. VLF radio waves are a type of electromagnetic wave propagating in the global "ground ionosphere" waveguide formed by the earth's surface and the lower ionosphere [6]. Due to the anisotropic dielectric properties of the lower ionosphere and its complex space–time variations, accurately predicting its propagation characteristics is challenging [7], especially in an abnormal solar activity period [8]. There is still a lack of more accurate algorithms for low ionosphere and VLF propagation, which has been a prominent research issue in recent years.

Research on the propagation characteristics of VLF radio waves dates back to the 1960s. The classical absorption curve, given by Helliwell (1965) [9], calculates the energy attenuation of VLF waves penetrating the ionosphere. This model has been utilized by Inan (1984) [10], Abel and Thorne (1998) [11], and Starks (2008) [12]. Helliwell (1965) employed

a model of the ionospheric D-region that is averaged and does not vary with latitude. However, the actual ionospheric D-region electron density does change with latitude and season and undergoes complex physical changes. Therefore, this model is only suitable for some instances of VLF wave propagation and preliminary qualitative analysis.

Considering that in the VLF band, the dielectric parameters of the lower ionosphere vary sharply within a wavelength range, ray theory is not suitable [13,14]. However, it can be considered to idealize the ionosphere into a horizontally layered medium, and the solution is obtained using the method of a whole-wave solution [15]. Budden (1985) [16] summarized early methods and pointed out that many of these methods face challenges in maintaining numerical calculation stability. Lehtinen and Inan (2009) [17] improved the full-wave solution method. However, the results still indicated that the model's predicted values significantly exceeded the VLF wave intensity measured at satellite altitudes, highlighting the model's lack of accuracy.

In 2014, Pan Wei yan and Li Kai combined their predecessors' work to systematically and comprehensively summarize and derive the propagation of very long waves in the ground ionospheric waveguide. They proposed W K. B. approximation and Airy function approximation to calculate height gain, which has promoted the development of very-long-wave propagation theory in China [18].

In 2016, Samanes, Raulin et al. combined measured data to study the effect of solar radiation on ionospheric height [19]. In 2018, Zhang Shui xian et al. calculated the predicted values of very-long-wave field strength under different ionospheric profiles, providing a reference for selecting the optimal ionospheric parameters [20]. In 2018, Tong He et al. calculated the multimode interference (MMI) and phase standard deviation of very-long-wave propagation in anisotropic Earth ionospheric waveguides [21].

Swati (2021) [22] and Forrest (2021) [8] both considered using the international reference ionosphere (International Reference Ionosphere, IRI) model to simulate the reflection parameters of the lower ionosphere and verified the viability of the VLF band under the IRI model. Richardson and Cohen studied the seasonal variation in the D-Region ionosphere and proposed the VLF propagation model based on Machine Learning [23].

In summary, in the field of VLF propagation, compared to Austin's empirical formula and wave jump theory, the waveguide mode method has higher computational accuracy and effectively overcomes the limitations of propagation distance. The above methods all use ionospheric data provided by IRI and these ionospheric parameters are isotropic [13]. The propagation of radio waves in the ionosphere is influenced by the geomagnetic field, and the ionosphere exhibits anisotropy. However, due to the need to transform simple scalar calculation problems into complex tensor-solving problems in the calculation of anisotropic media, the difficulty and complexity of the calculation increase sharply. To simplify the calculation, the ionosphere is often regarded as an isotropic medium in traditional methods, but this is clearly not in line with the actual situation, especially in some bands where anisotropy is significant. Ignoring this element will have a certain impact on the calculation results of radio wave propagation.

In order to further improve the accuracy of the waveguide mode algorithm, it is necessary to consider the influence of non-uniform anisotropy of the ionosphere on VLF waves. In this paper, a layered model structure of the lower ionosphere is established, considering ionospheric anisotropy. Firstly, the transmission matrix of the anisotropic layered structure is derived and verified. Then, the scattering characteristics of VLF electromagnetic waves in those above ionospheric layered structures under various conditions are accurately calculated based on the transmission matrix [24], and the propagation laws are summarized. In the comparative verification, we calculated the field strength of 17 kHz VLF electromagnetic waves within a transmission distance range of 500–1600 km based on the proposed method and compared it with the statistical data collected from actual communication experiments and the theoretical calculation results based on traditional ITU-R P.372-11. The results show that compared with the theoretical results based on ITU-R P.372-11, the method proposed in this paper fully considers the vertical height non-

uniformity of the ionosphere, and its calculated results are more consistent with actual measurement data, with higher accuracy. This work provides a robust calculation model for VLF propagation in the middle and lower ionosphere and significantly enhances the accuracy of its propagation and scattering calculations. It can offer valuable guidance and a reference for research on VLF electromagnetic wave propagation in the atmosphere.

2. Multilayer Anisotropic Ionospheric Model

The interior of the ionosphere is filled with free electrons, and the density of free electrons determines the electromagnetic parameters of the ionosphere. The density of free electrons in the ionosphere varies with vertical altitude, and the presence of the geomagnetic field induces electron spin [21], resulting in significant uneven electromagnetic anisotropy of the ionosphere with altitude. The above characteristics result in complex electromagnetic scattering of electromagnetic waves in the ionosphere.

In order to accurately analyze the scattering characteristics of electromagnetic waves in the ionosphere, we established an accurate ionospheric model at a vertical height (currently without considering the horizontal non-uniformity of the ionosphere), as shown in Figure 1. In the coordinate system of Figure 1, the z-axis represents the vertical height starting from the earth's surface, and the *xoy* plane is the bottom of the ionosphere, which is usually 75 km away from the earth's surface (this height varies with seasons and morning and evening, and needs to be determined according to actual seasons and time in specific calculations). Assuming that the geomagnetic field in the entire space is uniform, the entire non-uniform anisotropic ionosphere is horizontally divided into multiple layers along the z-axis, with each layer having the same height and being much smaller than the wavelength, ensuring that the electrons in each layer are present. The density is approximately uniform. In this way, the non-uniform anisotropic ionosphere is transformed into a multilayered anisotropic layered structure.
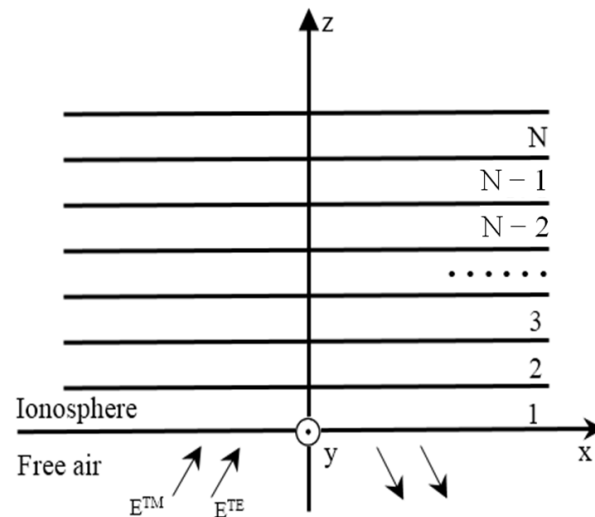

Figure 1. Horizontal multilayer anisotropic structure of ionospheric model.

Assuming the geomagnetic field's direction in Figure 1 to be arbitrary, with angles α, β, and γ representing its orientations along the *x*, *y*, and *z* axes, respectively, E^{TM} and E^{TE} represent two polarization forms of the electromagnetic waves, respectively, in Figure 1.

The permittivity of the ionosphere is $\bar{\varepsilon}$, and we have the following [25]:

$$\bar{\varepsilon} = \begin{bmatrix} \varepsilon_{xx} & \varepsilon_{xy} & \varepsilon_{xz} \\ \varepsilon_{yx} & \varepsilon_{yy} & \varepsilon_{yz} \\ \varepsilon_{zx} & \varepsilon_{zy} & \varepsilon_{zz} \end{bmatrix} \tag{1}$$

The elements in the matrix are as follows:

$$
\begin{aligned}
\frac{\varepsilon_{xx}}{\varepsilon_0} &= 1 + \frac{i\omega_0^2}{\omega(\nu-i\omega)} \frac{(\nu-i\omega)^2 + \omega_T^2 \cos^2\alpha}{(\nu-i\omega)^2 + \omega_T^2} \\
\frac{\varepsilon_{xy}}{\varepsilon_0} &= \frac{i\omega_0^2}{\omega(\nu-i\omega)} \frac{\omega_T^2 \cos\alpha\cos\beta - \omega_T\cos\gamma(\nu-i\omega)}{(\nu-i\omega)^2 + \omega_T^2} \\
\frac{\varepsilon_{xz}}{\varepsilon_0} &= \frac{i\omega_0^2}{\omega(\nu-i\omega)} \frac{\omega_T^2 \cos\alpha\cos\gamma + \omega_T\cos\beta(\nu-i\omega)}{(\nu-i\omega)^2 + \omega_T^2} \\
\frac{\varepsilon_{yx}}{\varepsilon_0} &= \frac{i\omega_0^2}{\omega(\nu-i\omega)} \frac{\omega_T^2 \cos\alpha\cos\beta + \omega_T\cos\gamma(\nu-i\omega)}{(\nu-i\omega)^2 + \omega_T^2} \\
\frac{\varepsilon_{yy}}{\varepsilon_0} &= 1 + \frac{i\omega_0^2}{\omega(\nu-i\omega)} \frac{(\nu-i\omega)^2 + \omega_T^2 \cos^2\beta}{(\nu-i\omega)^2 + \omega_T^2} \\
\frac{\varepsilon_{yx}}{\varepsilon_0} &= \frac{i\omega_0^2}{\omega(\nu-i\omega)} \frac{\omega_T^2 \cos\gamma\cos\beta - \omega_T\cos\alpha(\nu-i\omega)}{(\nu-i\omega)^2 + \omega_T^2} \\
\frac{\varepsilon_{zx}}{\varepsilon_0} &= \frac{i\omega_0^2}{\omega(\nu-i\omega)} \frac{\omega_T^2 \cos\gamma\cos\alpha - \omega_T\cos\beta(\nu-i\omega)}{(\nu-i\omega)^2 + \omega_T^2} \\
\frac{\varepsilon_{zy}}{\varepsilon_0} &= \frac{i\omega_0^2}{\omega(\nu-i\omega)} \frac{\omega_T^2 \cos\gamma\cos\beta + \omega_T\cos\alpha(\nu-i\omega)}{(\nu-i\omega)^2 + \omega_T^2} \\
\frac{\varepsilon_{zz}}{\varepsilon_0} &= 1 + \frac{i\omega_0^2}{\omega(\nu-i\omega)} \frac{(\nu-i\omega)^2 + \omega_T^2 \cos^2\gamma}{(\nu-i\omega)^2 + \omega_T^2}
\end{aligned}
\tag{2}
$$

where ω is the frequency of incident wave, ω_0 is plasma frequency, ω_T is magnetic rotation frequency and ν is collision frequency. Here, H_0 is the intensity of the geomagnetic field, N_0 is the electron density, m_e is the electron mass, and e is the charge. The values of N_0 and ν can be queried through the IRI.

Here, the following hold:

$$
\omega_0{}^2 = (N_0 e^2)/(m_e \varepsilon_0), \quad \omega_T = (\mu_0 e H_0)/m_e
\tag{3}
$$

In the following sections, we will systematically address this model and derive a transfer matrix applicable to any anisotropic medium, drawing upon the principles of the transfer matrix method.

3. Transfer Matrix Method

3.1. Theoretical Derivation

We conducted in-depth research on electromagnetic propagation in anisotropic multilayer structures for the anisotropic ionosphere. As the electromagnetic parameters of anisotropic multilayer media manifest as tensors, they introduce complexity to the electromagnetic field within the structure, rendering the calculation of its electromagnetic characteristics a challenging endeavor. To address this complexity, we draw upon the concept of a transfer matrix. This allows us to meticulously derive multilayer structures' electromagnetic wave transmission characteristics comprising arbitrary anisotropic materials. We achieve this by comprehensively analyzing and calculating various anisotropic media [26].

Constructing a multilayer structure composed of a series of uniformly anisotropic media with equal thickness is depicted in Figure 2. Assuming the number of layers is N, the electromagnetic parameters of each layer are different, which can be expressed as $[\varepsilon_{ij}]$ and $[\mu_{ij}]$ (i, j = 1, 2, 3), respectively. The thickness of each layer is d. The EM wave is incident at any angle of θ, and the *xoz* plane is the incident plane. We can obtain the eigen equation of the EM field in the Mth layer material [26].

$$
\mathbf{A} \cdot \begin{bmatrix} E_x \\ E_y \\ H_y \\ H_x \end{bmatrix} = \boldsymbol{\gamma} \cdot \begin{bmatrix} E_x \\ E_y \\ H_y \\ H_x \end{bmatrix}
\tag{4}
$$

where **A** is a Berreman matrix:

$$
\begin{bmatrix}
-\delta\frac{\varepsilon_{13}}{\varepsilon_{33}} & \delta\left(\frac{\mu_{23}}{\mu_{33}}-\frac{\varepsilon_{23}}{\varepsilon_{33}}\right) & \mu_{22}-\frac{\mu^2_{23}}{\mu_{33}}-\frac{\delta^2}{\varepsilon_{33}} & -\mu_{12}+\frac{\mu_{13}\mu_{23}}{\mu_{33}} \\
0 & -\delta\frac{\mu_{13}}{\mu_{33}} & -\mu_{12}+\frac{\mu_{13}\mu_{23}}{\mu_{33}} & \mu_{11}-\frac{\mu^2_{13}}{\mu_{33}} \\
\varepsilon_{11}-\frac{\varepsilon^2_{13}}{\varepsilon_{33}} & \varepsilon_{12}-\frac{\varepsilon_{13}\varepsilon_{23}}{\varepsilon_{33}} & -\delta\frac{\varepsilon_{13}}{\varepsilon_{33}} & 0 \\
\varepsilon_{12}-\frac{\varepsilon_{13}\varepsilon_{23}}{\varepsilon_{33}} & \varepsilon_{22}-\frac{\varepsilon^2_{23}}{\varepsilon_{33}}-\frac{\delta^2}{\mu_{33}} & \delta\left(\frac{\mu_{23}}{\mu_{33}}-\frac{\varepsilon_{23}}{\varepsilon_{33}}\right) & -\delta\frac{\mu_{13}}{\mu_{33}}
\end{bmatrix}
$$

where ε_{ij}, μ_{ij} (i,j = 1,2,3) are the elements in a matrix of $[\varepsilon_{ij}]$ and $[\mu_{ij}]$, and $\delta = \sin\theta$.
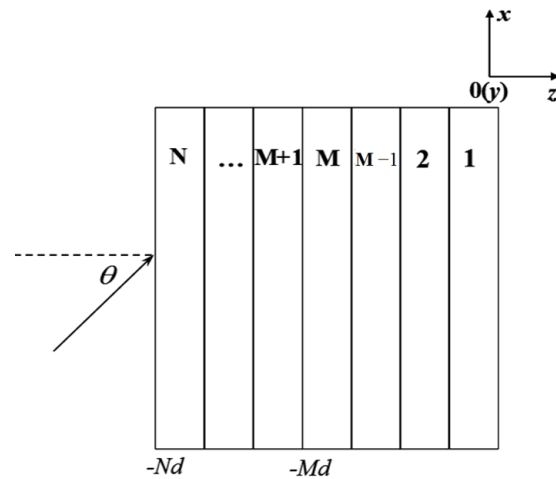

Figure 2. Anisotropic horizontal layered multilayer media structure.

Assume the eigenvalues and eigenvectors of Formula (4) are $\gamma_{(M)}$ and $\mathbf{W}_{(M)}$ (4 × 4 matrix), respectively, where $\gamma_{(M)} = [\gamma_{(M)1}, \gamma_{(M)2}, \gamma_{(M)3}, \gamma_{(M)4}]$ and $\gamma_{(M)1}$ and $\gamma_{(M)2}$ are greater than 0, while $\gamma_{(M)3}$ and $\gamma_{(M)4}$ are less than 0. Where $\gamma_{(M)1}$ represents the type I incident wave, $\gamma_{(M)3}$ represents the type I reflected wave, $\gamma_{(M)2}$ represents the type II incident wave, and $\gamma_{(M)4}$ represents the type II reflected wave, the field distribution in the M-layer region can be expressed as follows:

$$
\begin{bmatrix}
E_{(M)x} \\
E_{(M)y} \\
\eta H_{(M)y} \\
-\eta H_{(M)x}
\end{bmatrix}
= \mathbf{W}_{(M)} \cdot \mathbf{X}_{(M)} \cdot \mathbf{G} \cdot
\begin{bmatrix}
u_{(M)1} \\
u_{(M)2} \\
v_{(M)1} \\
v_{(M)2}
\end{bmatrix}
\tag{5}
$$

Here, η is wave impedance in free space, $\mathbf{X}_{(M)}$ is a diagonal array matrix, and its internal elements are $X_{(M)}(j,j) = \exp(k_0\gamma_{(M)j}(z+(M-1)d))$, ($j$ = 1,2,3,4); $\mathbf{G}$ is another diagonal array matrix and its internal elements are $G(j,j) = \exp(k_0(x\,\delta))$; $u_{(M)1}$ and $v_{(M)1}$ are the amplitudes of the upper waves of the TE wave and TM wave in the Mth layer, and $u_{(M)2}$ and $v_{(M)2}$ are the amplitudes of the down waves of the TE wave and TM wave in the Mth layer, respectively.

Similarly, the fields in the (M − 1) layer and the (M + 1) layer can be represented as follows:

$$
\begin{bmatrix}
E_{(M-1)x} \\
E_{(M-1)y} \\
\eta H_{(M-1)y} \\
-\eta H_{(M-1)x}
\end{bmatrix}
= \mathbf{W}_{(M-1)} \cdot \mathbf{X}_{(M-1)} \cdot \mathbf{G} \cdot
\begin{bmatrix}
u_{(M-1)1} \\
u_{(M-1)2} \\
v_{(M-1)1} \\
v_{(M-1)2}
\end{bmatrix}
\tag{6}
$$

and

$$
\begin{bmatrix} E_{(M+1)x} \\ E_{(M+1)y} \\ \eta H_{(M+1)y} \\ -\eta H_{(M+1)x} \end{bmatrix} = \mathbf{W}_{(M+1)} \cdot \mathbf{X}_{(M+1)} \cdot \mathbf{G} \cdot \begin{bmatrix} u_{(M+1)1} \\ u_{(M+1)2} \\ v_{(M+1)1} \\ v_{(M+1)2} \end{bmatrix} \tag{7}
$$

Here, $X_{(M-1)}(j,j)$ is $\exp(k_0\gamma_{(M)j}(z+(M-2)d))$ and $X_{(M+1)}(j,j)$ is $\exp(k_0\gamma_{(M)j}(z+Md))$, ($j$ = 1,2,3,4).

The field at z = $-$ (M $-$ 1)d has the following relationship:

$$
\mathbf{W}_{(M-1)} \cdot \mathbf{X}_{(M-1)} \cdot \begin{bmatrix} u_{(M-1)1} \\ u_{(M-1)2} \\ v_{(M-1)1} \\ v_{(M-1)2} \end{bmatrix} = \mathbf{W}_{(M)} \cdot \begin{bmatrix} u_{(M)1} \\ u_{(M)2} \\ v_{(M)1} \\ v_{(M)2} \end{bmatrix} = \mathbf{P} \tag{8}
$$

The field at z = $-$Md has the following relationship:

$$
\mathbf{W}_{(M)} \cdot \mathbf{X}_{(M)} \cdot \begin{bmatrix} u_{(M)1} \\ u_{(M)2} \\ v_{(M)1} \\ v_{(M)2} \end{bmatrix} = \mathbf{W}_{(M+1)} \cdot \begin{bmatrix} u_{(M+1)1} \\ u_{(M+1)2} \\ v_{(M+1)1} \\ v_{(M+1)2} \end{bmatrix} = \mathbf{Q} \tag{9}
$$

By Equations (8) and (9), the relationship between the interfaces on both sides of the M-layer can be established:

$$
\mathbf{Q} = \mathbf{W}_{(M)} \cdot \mathbf{X}_{(M)} \cdot \mathbf{W}_{(M)}^{-1} \cdot \mathbf{P} \tag{10}
$$

Obviously, the matrix $\mathbf{T}_{(M)} = \mathbf{W}_{(M)} \cdot \mathbf{X}_{(M)} \cdot \mathbf{W}_{(M)}^{-1}$ is the transfer matrix of the Mth-layer medium, which establishes the connection between the fields on both sides of the Mth-layer. The total transmission matrix of the multilayer structure in Figure 2 can be obtained via the following:

$$
\mathbf{T} = \mathbf{T}_{(1)} \times \mathbf{T}_{(2)} \times \dots \mathbf{T}_{(N-1)} \times \mathbf{T}_{(N)} \tag{11}
$$

The feature vectors in free space are as follows:

$$
\mathbf{W}_{(0)} = \begin{bmatrix} \beta & 0 & \beta & 0 \\ 0 & 1 & 0 & 1 \\ 1 & 0 & -1 & 0 \\ 0 & \beta & 0 & -\beta \end{bmatrix} \tag{12}
$$

Here, $\beta = \cos\theta$.

At z = 0, there are only transmitted waves and no reflected waves. Then, the relationship between the free space field at z = $-Nd$ and the field at z = 0 is as follows:

$$
\mathbf{W}_{(0)} \cdot \begin{bmatrix} u_{(0)1} \\ u_{(0)2} \\ v_{(0)1} \\ v_{(0)2} \end{bmatrix} = \mathbf{T} \cdot \mathbf{W}_{(0)} \cdot \begin{bmatrix} u_{(1)1} \\ u_{(1)2} \\ 0 \\ 0 \end{bmatrix} \tag{13}
$$

and

$$
\begin{bmatrix} u_{(0)1} \\ u_{(0)2} \\ v_{(0)1} \\ v_{(0)2} \end{bmatrix} = \mathbf{F} \cdot \begin{bmatrix} u_{(1)1} \\ u_{(1)2} \\ 0 \\ 0 \end{bmatrix} \tag{14}
$$

where

$$\mathbf{F} = \mathbf{W}_{(0)}^{-1} \cdot \mathbf{T} \cdot \mathbf{W}_{(0)}$$

Then, we have the following:

$$\begin{bmatrix} v_{(0)1} \\ v_{(0)2} \end{bmatrix} = \begin{bmatrix} R_{11} & R_{12} \\ R_{21} & R_{22} \end{bmatrix} \begin{bmatrix} u_{(0)1} \\ u_{(0)2} \end{bmatrix} \tag{15}$$

The reflection matrix R can be obtained from Equation (15).

$$\mathbf{R} = \begin{bmatrix} R_{11} & R_{12} \\ R_{21} & R_{22} \end{bmatrix} \tag{16}$$

The matrix R represents a generalized reflection coefficient encompassing multiple optical reflection processes. Within this matrix, there are four elements, all of which are complex. R_{11} is the reflection coefficient of a type I wave reflected into another type I wave, R_{22} is the reflection coefficient of a type II wave reflected into yet another type I wave. R_{12} and R_{21} are the reflection coefficients of a type I wave reflected into a type II wave and a type II wave reflected into a type I wave, respectively. These coefficients capture the coupling characteristics between type I waves and type II waves.

3.2. Method Validation

To verify the correctness of the transmission matrix method, we designed a simulation experiment to compare the traditional optical method [24] with the transmission matrix method. The optical method is referred to as method 1, and the transfer matrix method is referred to as method 2.

Firstly, we designed a multilayered periodic isotropic layered medium as shown in Figure 3, assuming that all media were non-magnetic. The medium consists of five identical units, each unit divided into two main parts. The first part consists of two alternating media with dielectric constants of ε_{r1} and ε_{r2}, respectively. The second part consists of two alternating media with dielectric constants of ε_{r3} and ε_{r4}, respectively.
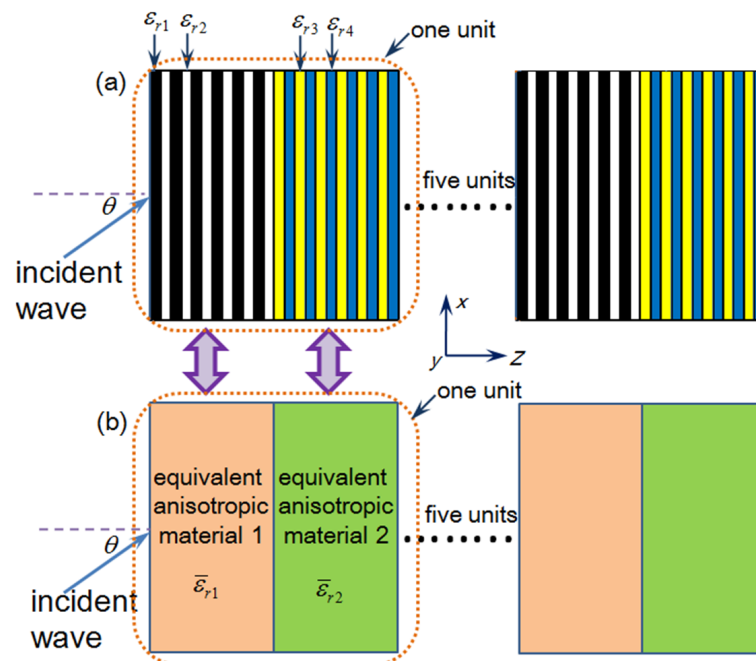

Figure 3. (**a**) Multilayer isotropic periodic media before equivalence. (**b**) Equivalent multilayer anisotropic periodic media.

In the traditional optical method (method 1) [27,28], the transmission matrix of isotropic media 1 is as follows:

$$\mathbf{M}_1 = \begin{pmatrix} \cos(k_0 n_1 d_1 \cos\theta_1) & -\frac{i}{p_1}\sin(k_0 n_1 d_1 \cos\theta_1) \\ -ip_1 \sin(k_0 n_1 d_1 \cos\theta_1) & \cos(k_0 n_1 d_1 \cos\theta_1) \end{pmatrix} \tag{17}$$

Here, $p_1 = \sqrt{\frac{\varepsilon_{r1}\varepsilon_0}{\mu_{r1}\mu_0}}\cos\theta_1, n_1 = \sqrt{\varepsilon_1\mu_1}$, and d_1 is the thickness of media 1.k0 is the wave number in free space.

Similarly, the transmission matrices of media 2, 3, and 4 are, respectively, the following:

$$\mathbf{M}_2 = \begin{pmatrix} \cos(k_0 n_2 d_2 \cos\theta) & -\frac{i}{p_2}\sin(k_0 n_2 d_2 \cos\theta) \\ -ip_2 \sin(k_0 n_2 d_2 \cos\theta) & \cos(k_0 n_2 d_2 \cos\theta) \end{pmatrix} \tag{18}$$

$$\mathbf{M}_3 = \begin{pmatrix} \cos(k_0 n_3 d_3 \cos\theta) & -\frac{i}{p_3}\sin(k_0 n_3 d_3 \cos\theta) \\ -ip_3 \sin(k_0 n_3 d_3 \cos\theta) & \cos(k_0 n_3 d_3 \cos\theta) \end{pmatrix} \tag{19}$$

$$\mathbf{M}_4 = \begin{pmatrix} \cos(k_0 n_4 d_4 \cos\theta) & -\frac{i}{p_4}\sin(k_0 n_4 d_4 \cos\theta) \\ -ip_4 \sin(k_0 n_4 d_4 \cos\theta) & \cos(k_0 n_4 d_4 \cos\theta) \end{pmatrix} \tag{20}$$

The transmission matrix of the whole structure in Figure 3a is

$$\mathbf{M} = ((\mathbf{M}_1 \times \mathbf{M}_2)^a \times (\mathbf{M}_3 \times \mathbf{M}_4)^b)^5 = \begin{bmatrix} m_{11} & m_{12} \\ m_{21} & m_{22} \end{bmatrix} \tag{21}$$

Here, a is the number of layers for medium 1 and medium 2 in unit 1 and b is the number of layers for medium 1 and medium 2 in unit 1.

The reflection coefficient calculated by the optical method is as follows [25]

$$R_{11} = \frac{(m_{11} + m_{12}p_4)p_1 - (m_{21} + m_{22}p_4)p_1}{(m_{11} + m_{12}p_4)p_1 + (m_{21} + m_{22}p_4)p_1} \tag{22}$$

According to the equivalent medium theory, if the thickness of the film is far less than the wavelength, the periodic multilayer film material can be equivalent to a uniaxial anisotropic medium. The structure of Figure 3a is equivalent to a multilayer structure composed of five sets of anisotropic media as shown in Figure 3b [24]. The equivalent permittivity of the alternating structure of media 1 and 2 is as follows:

$$\bar{\varepsilon}_{r1} = \begin{bmatrix} \varepsilon_{s1} & 0 & 0 \\ 0 & \varepsilon_{s1} & 0 \\ 0 & 0 & \varepsilon_{z1} \end{bmatrix} \tag{23}$$

Here, $\varepsilon_{s1} = \frac{\varepsilon_{r1}\varepsilon_0 + \varepsilon_{r2}\varepsilon_0 \alpha}{1+\alpha}$, $\frac{1}{\varepsilon_{z1}} = \frac{1}{\varepsilon_{r1}\varepsilon(1+\alpha)} + \frac{\alpha}{\varepsilon_{r2}\varepsilon(1+\alpha)}$, and $\alpha = \frac{d_1}{d_2}$.

Similarly, the equivalent permittivity of the alternating structure of media 3 and 4 can be obtained.

The reflection coefficient can be obtained by taking the equivalent permittivity into the transfer matrix method in the previous section (method 2).

As an example, we can arbitrarily choose the values of ε_{r1}, ε_{r2}, ε_{r3}, and ε_{r4}. Here, $\varepsilon_{r1} = 1.2$, $\varepsilon_{r2} = 1.5$, $\varepsilon_{r3} = 2.1$, and $\varepsilon_{r4} = 0.8$; $d_1{:}d_2{:}d_3{:}d_4$ is 1:1:1.5:1.2.

We calculated the reflection coefficient of the structure in Figure 3 using method 1 and method 2, respectively. The outcomes of these calculations are presented in Figure 4. Figure 4a shows the calculation structure with an incident angle of 0 degrees ($\theta = 0°$) and Figure 4b shows the calculation structure with an incident angle of 60 degrees ($\theta = 60°$). Notably, the results obtained from both methods exhibit a substantial degree of consistency. This consistency serves as strong evidence for the validity and correctness of the transfer matrix method that we have developed in this research.
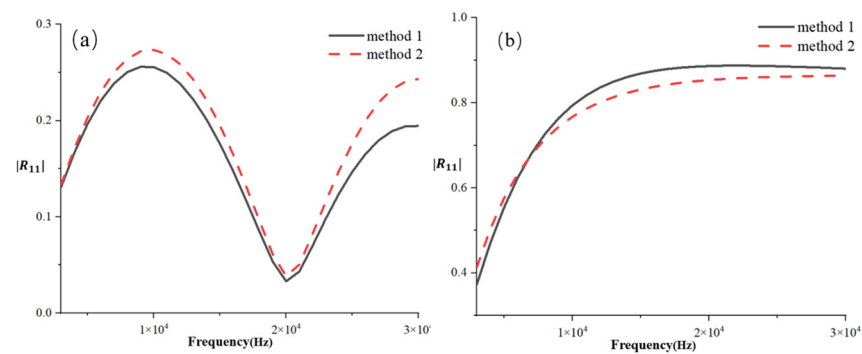
Figure 4. The reflection coefficient of periodically stratified media with different frequency. (**a**) θ = 0°; (**b**) θ = 60°.

In addition, we compared the reflection coefficients of the whole structure under different values and incident angles using methods 1 and 2, and the results calculated by the two methods were still in good agreement. It can be seen that the transmission matrix proposed in this article is correct.

4. Numerical Calculation and Analysis

4.1. Layer Thickness Selection

In actual radio wave propagation, the VLF band mainly relies on the lower ionosphere, and the dielectric parameters of the lower ionosphere vary sharply within a height range of one wavelength of VLF. Therefore, selecting the appropriate layering method, especially the layering thickness, is a crucial part of the calculation.

In the ideal case, a more detailed ionospheric model brings it closer to reality, resulting in a higher calculation accuracy. However, this comes at the cost of increased computational complexity. In practical use, it is essential to strike a balance between calculation efficiency and accuracy to obtain the optimal solution. Taking a specific time and location as an example, the range of the lower ionospheric height is 60 km–150 km. Based on the IRI model, the data acquisition interface is illustrated in Figure 5. Ionospheric parameters with layer thicknesses d of 0.3 km, 0.5 km, 1 km, 5 km, and 10 km are obtained, respectively. Models are established, and the reflection coefficient R_{11} is calculated. Note that R_{11} represents the modulus of R_{11}, which is the absolute value of the reflection coefficient of the type I wave reflected into the type I wave.

Figure 5. IRI data export interface.

As illustrated in Figure 6, under the condition that other factors remain unchanged, with the decrease in thickness of d, the calculation results gradually tend to be consistent. When d drops to 1 km or less, the reflection coefficient curve is essentially consistent. Considering both calculation efficiency and the potential for numerical overflow, it is reasonable to set the layer thickness d as 1 km. It should be noted that our algorithm involves a large number of matrix operations. During the calculation process using MATLAB 8.0, we found

that when d is greater than 0.5, the program runs normally and the results are reliable. If d is too small, the program will report an error, resulting in unreliable calculation results. Therefore, we only present curves with d greater than 0.3. The above content is explained in the revised version, and we will further optimize the program in the future.
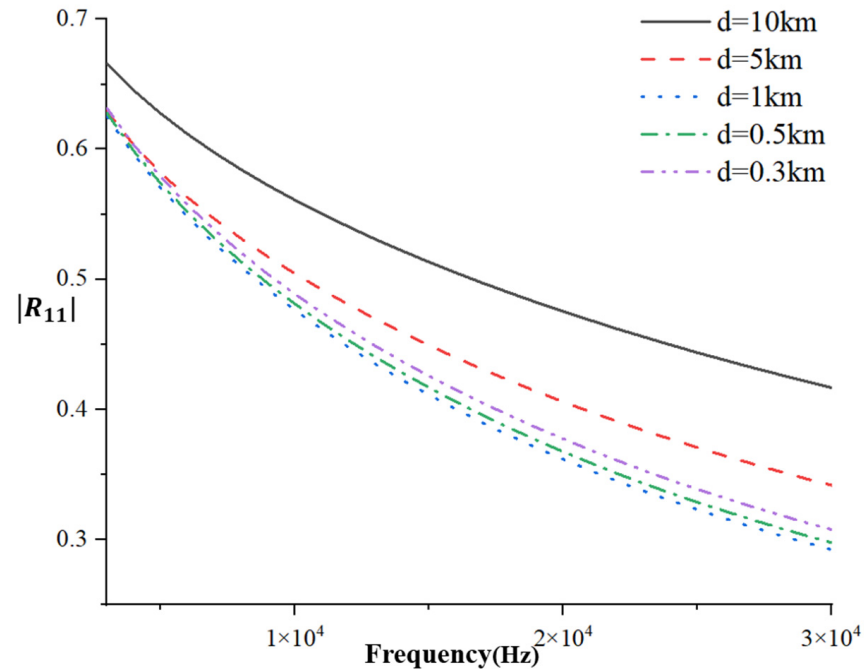

Figure 6. The curve of reflection coefficient R11 changes with frequency under different delimitation thicknesses.

4.2. Calculation Results and Analysis

Once the thickness of the ionospheric model layers is determined, this section proceeds to establish the model, calculate the reflection coefficient, and study the VLF propagation law. The ionospheric parameters include electron concentration and collision frequency, while the geomagnetic parameters include geomagnetic intensity, geomagnetic dip angle, and declination angle. These parameters vary with geographical location, altitude, season, and local time. Therefore, the ionospheric parameters in this paper are derived from the calculation results of the International Geomagnetic Reference Field(IGRF) and the IRI.

According to Figure 7, the height of the ionosphere at night in winter is about 20 km higher than that in day. At the same height, the electron density in the lower ionosphere at night in summer is much higher than that in winter. This phenomenon is related to direct sunlight. The greater the solar radiation, the more active the ionosphere, resulting in higher electron concentration.

It can be seen from Figure 8 that the reflection coefficient at night is significantly lower than during the daytime and slightly lower in summer compared to winter. According to the electron density map, a higher electron density corresponds to a higher reflection coefficient. In other words, the propagation efficiency of the VLF band is higher during the daytime than at night, and the propagation effect is better in summer compared to winter.

When studying the influence of collision frequency on the reflection coefficient, the fixed value of the geomagnetic dip angle is $45°$, the angle of incidence θ takes $30°$, and the collision frequency is $10^7 \text{ s}^{-1}, 10^6 \text{ s}^{-1}, 10^5 \text{ s}^{-1}$. On the other hand, when studying the influence of the incident angle on the reflection coefficient, the fixed frequency is 5 kHz, the collision frequency is 10^6 s^{-1}, and the incident angles are $0°$, $30°$, and $60°$.

The main diagonal element R_{11} of the reflection matrix represents the reflection coefficient of the incident TM wave reflected into the TM wave, and R_{22} represents the reflection coefficient of the incident TE wave reflected into the TE wave.
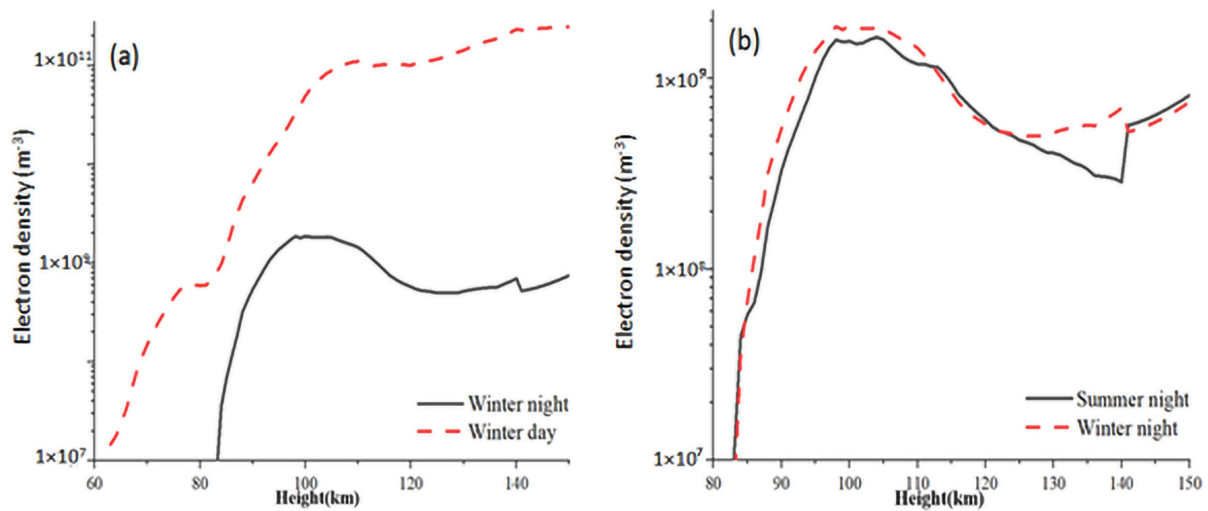
Figure 7. (**a**) Curve of electron concentration with height on winter night and winter day. (**b**) Curve of electron concentration with height in summer and winter night.
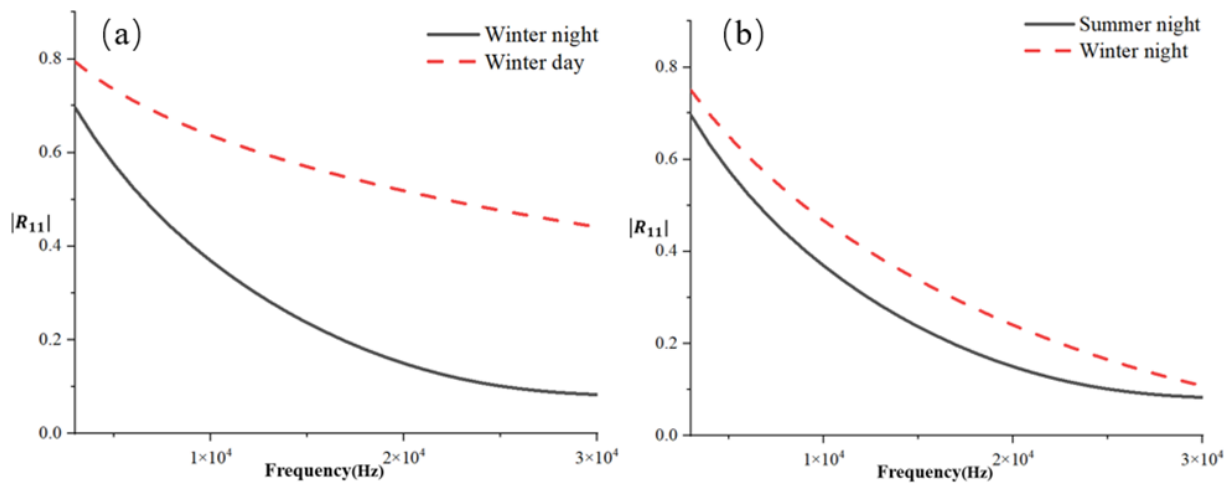

Figure 8. (**a**) Curve of reflection coefficient with frequency at night and during day. (**b**) Curve of reflection coefficient with frequency in summer and winter.

As shown in Figure 9, with the increase in electron collision frequency and incident wave frequency, the reflection coefficient R_{11} decreases. When the collision frequency v increases from 10^5 s^{-1} to 10^6 s^{-1}, the reflection coefficient decreases significantly, indicating that the more active the ionosphere is, the worse the electromagnetic wave reflection effect of the ionosphere on the VLF band becomes.

As shown in Figure 10, the reflection coefficient of the TM wave decreases with the increase in incident angle, while the TE wave exhibits the opposite trend. This phenomenon is related to the polarization direction of the two kinds of electromagnetic waves.

Assume the dip angle is the angle between the geomagnetic field and the vertical direction, which is complementary to the geomagnetic dip angle. As shown in Figure 11, the reflection coefficient R_{11} increases with the dip angle from 0° to 180°. The reflection coefficient increases when the dip angle is less than 90° in the range of 0° to 90°. At 90°, it reaches its maximum value. This indicates that the reflection effect is best at the magnetic equator and worst at the magnetic poles. For the TE wave, its behavior is close to a straight line when the dip angle changes. In other words, the geomagnetic dip angle has little effect on the reflection. The reflection coefficient of the TE wave increases with the increase in the incidence angle, which is opposite to the behavior of the TM wave and consistent with the trend illustrated in Figure 10.
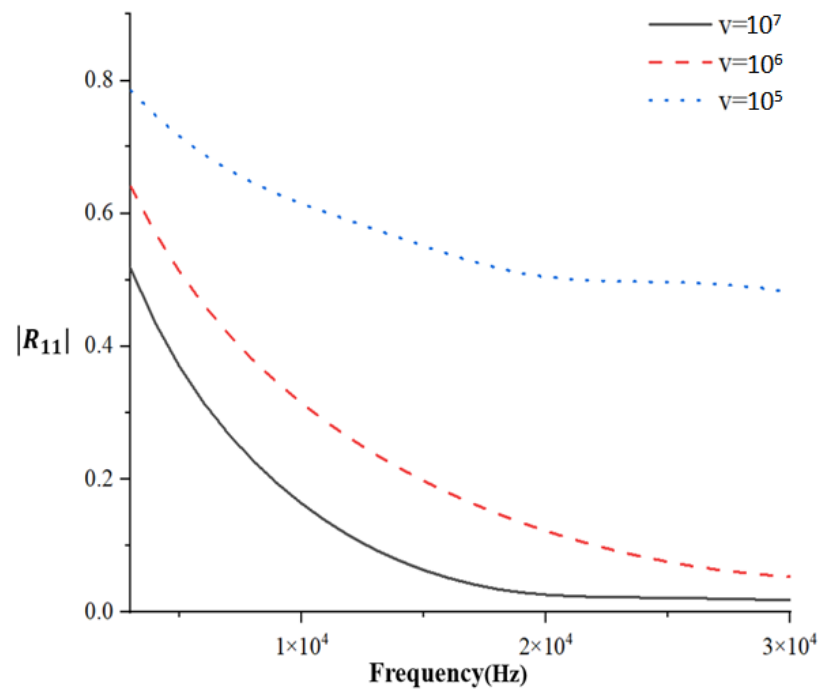
Figure 9. R11 with frequency when collision frequency is 10^7 s^{-1}, 10^6 s^{-1}, and 10^5 s^{-1}.
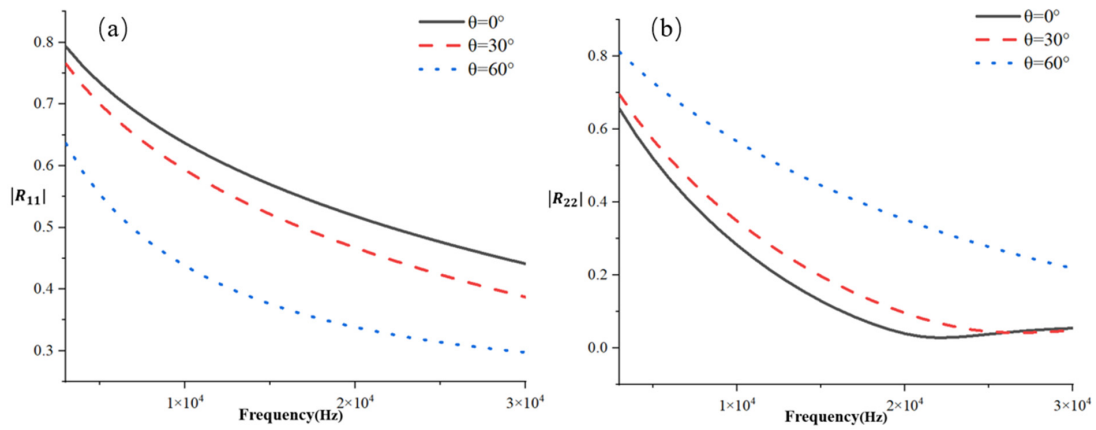

Figure 10. (**a**) R11 with frequency when incident angle is $0°,30°$, and $60°$. (**b**) R22 with frequency when incident angle is $0°$, $30°$, and $60°$.
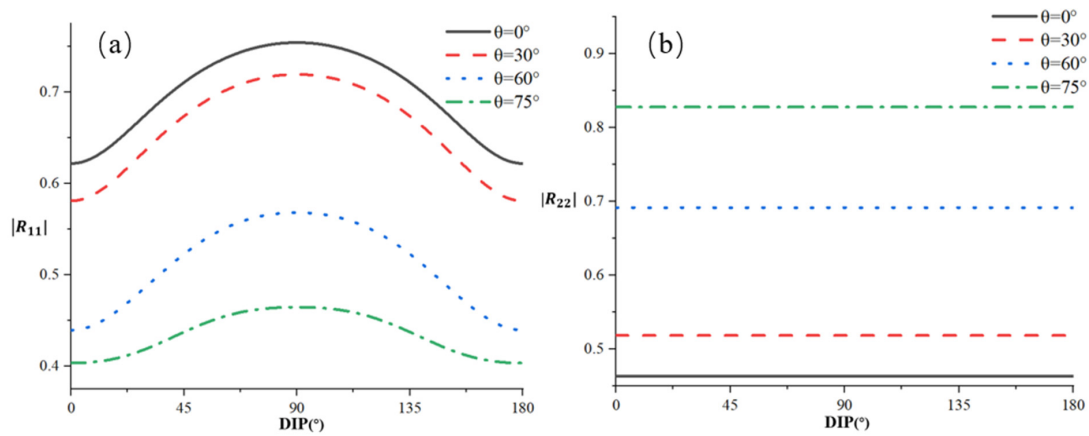

Figure 11. (**a**) R11 with frequency when dip angle is $0°$, $30°$, $60°$, and $75°$. (**b**) R22 with frequency when dip angle is $0°$, $30°$, $60°$, and $75°$.

In practical calculations, it is found that the values of R_{12} and R_{21} in the reflection matrix are very small and can be ignored. The coupling between the TE wave and the TM wave is minimal in the VLF band.

In summary, VLF exhibits the following propagation patterns in the anisotropic ionospheric model:

(1)   The anisotropy caused by the geomagnetic field in the very-long-wave frequency band can lead to a decrease in the ionosphere's ability to reflect radio waves and an increase in ionospheric absorption losses.

(2)   Overall, the reflection coefficient decreases with increasing frequency, and most of the time, the propagation laws of horizontally polarized waves and vertically polarized waves are opposite, which is related to the polarization direction of both. This article mainly analyzes horizontally polarized waves.

(3)   Both diurnal and seasonal variations can have an impact on the propagation of VLF in the ionosphere, with diurnal variations having a greater impact than seasonal variations. The propagation ability in summer is higher than that in winter, and the propagation ability in day is higher than that in night.

(4)   When other conditions remain unchanged, the higher the collision frequency, the greater the absorption loss of the ionosphere towards VLF. In the currently selected model, when v increases to the order of time, the reflection coefficient will undergo a sudden decrease, that is, in the VLF band. The reflection characteristics of the ionosphere towards radio waves are very sensitive to the activity of particles in the ionosphere.

(5)   In the same scenario, as the incident angle increases, the ionosphere's ability to reflect horizontally polarized waves of VLF increases, while the pattern of vertically polarized waves is opposite.

(6)   Under the same other conditions, the DIP (geomagnetic inclination angle) and VLF's horizontal polarized wave reflection ability in the ionosphere form a symmetrical structure at 0°–180°, with the strongest reflection ability at 90° and the weakest at 0° and 180°. When other conditions are the same, the reflection ability in low-latitude areas is higher than that in high-latitude areas.

(7)   In a horizontally uniform ionospheric model, the anisotropy of the ionosphere has a greater impact on east–west propagation compared to north–south propagation, and the direction originating from the geomagnetic field is close to the north–south distribution.

4.3. Calculation Examples

To verify the correctness of this method, we used it to calculate two practical examples and compared the calculated values with the statistical values we measured in recent years.

In this case, the latitude and longitude of the launch point are N37.38° and E112.12°, respectively. The latitude and longitude of the receiving point are N18.20° and E109.02°. The launch point is approximately 2000 km away from the receiving point. The transmission power is 50 kW. The efficiency of the transmitting antenna is 40%. The frequency is 17 kHz. The time is summer noon (12:00). We establish observation points every 200 km within the range of 600–1600 km.

According to public reports, the propagation area of very-low-frequency electromagnetic waves can be roughly divided into three regions, namely the ground wave mode region (0–400 km), the sky wave mode region (400 km–1600 km), and the waveguide mode region. In the propagation area of sky wave, the main jump mode of electromagnetic waves is one.

The ionosphere does exhibit non-uniformity in both the horizontal and vertical directions, but it is difficult to derive and calculate from considering these two aspects. Referring to the ionospheric statistical data of the ITU, we found that the non-uniformity of the ionosphere varies dramatically in the vertical direction, while it changes gently in the horizontal direction. Therefore, we currently only consider the non-uniformity of the ionosphere in

the vertical direction. Of course, this will result in our algorithm being unable to accurately calculate large electromagnetic propagation distances. Based on our calculations and actual measurement experience, our algorithm's current calculation results are relatively accurate within the range of 500–1600 km.

At present, we have successfully developed VLF propagation prediction software (which has been patented). The black stars in Figure 12 are the field strength values calculated by the software based on the above conditions. The values in the sky wave mode area (600–1600 km) were calculated using the method proposed in this paper. The red dots in Figure 12 represent the measurement statistics values in this area and the blue squares present the values were calculated by the traditional ITU-R P.372-11. By comparison, it can be seen that the calculated results using the proposed method are more matching with the measured values than the traditional ITU-R P.372-11, which proves our method is closer to the actual situation compared to traditional ITU-R P.372-11. In addition, it can also be observed in Figure 12 that within the range of 500–1000 km, our calculated values are very close to the actual measured values. However, beyond 1000 km, deviations begin to appear between them, and as the distance increases, the deviation also increases. We observe that the global distribution of the ionosphere is not only uneven in the vertical direction, but also in the horizontal direction. Currently, our method only considers the uneven distribution of the ionosphere in the vertical direction and does not take into account its horizontal distribution. Therefore, when the propagation distance (D) of electromagnetic waves in the ionosphere is small (D < 1000 Km), the electromagnetic scattering is less affected by the unevenness of the ionosphere in the horizontal direction, and the calculated results are in good agreement with the test results. As the propagation distance of electromagnetic waves increases, the unevenness of the ionosphere in the horizontal direction becomes prominent, leading to deviations in the calculated results.
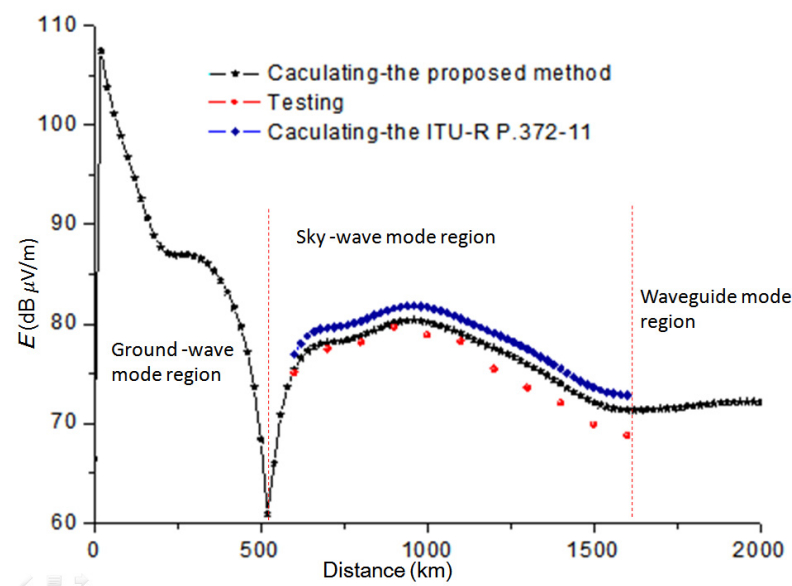

Figure 12. Comparison between theoretical calculations and actual measurement statistics at noon (12:00) in summer with a frequency of 17 kHz.

Then, we changed the frequency and compared the field strength of the receiving point at a distance of 800 km as shown in Figure 13. Subsequently, we changed the frequency and compared the field strength of the receiving point at a distance of 800 km. In Figure 13, the black square represents the calculated value, and the red sphere represents the measurement statistics values. It can be seen that the above two are basically consistent. The results in Figures 12 and 13 confirm the correctness of this algorithm and that it can be used for VLF propagation calculation. It should be pointed out that due to insufficient consideration

of additional losses such as ground reflection loss in this algorithm, the actual measured values are generally slightly smaller than the calculated values.
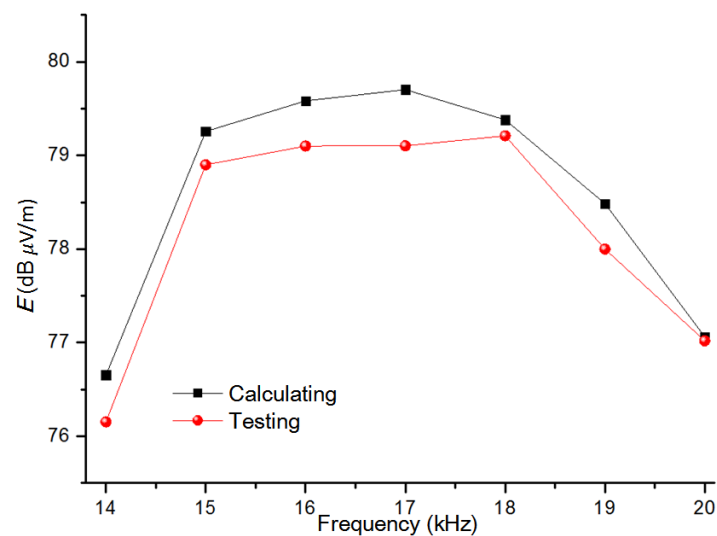

Figure 13. Comparison between theoretical calculations and actual measurement statistics at noon (12:00) in summer with different frequency.

On the propagation path of 2000 km, our measurement points are scattered, with a measurement radius of 50–100 km for each measurement point. Figure 12 shows the theoretical values are basically consistent with the measured statistical values which proves the correctness of our method.

5. Conclusions

In this paper, we derive a transfer matrix method based on the full-wave method and establish a more accurate anisotropic ionospheric model. Through calculation and verification, we determine a more suitable layering method. Using a specific location as an example, we calculate the reflection coefficient of VLF band electromagnetic waves in the lower ionosphere. We study the impact of incident wave frequency, incident angle, geomagnetic dip angle, frequency, ionospheric electron concentration, and electron collision frequency on ionospheric radio wave propagation. The comparative analysis results show that the calculation results using the proposed method are well matching with the testing results within the range of 500–1500 km, which can provide a good reference for engineering calculations within this distance range. At present, due to the fact that this method only considers the vertical non-uniformity of the ionosphere, it can ensure calculation accuracy within the range of 500–1500 km. Next, we will further improve the proposed method in this paper while fully considering the horizontal non-uniformity of the ionosphere and the curvature of the earth.

References

1. Barr, R.; Jones, D.L.; Rodger, C.J. ELF and VLF radio waves. *J. Atmos. Sol.-Terr. Phys.* **2000**, *62*, 1689–1718. [CrossRef]
2. Wang, J. Observation and analysis of phase cycle slipping of VLF signals. *Chin. J. Radio Sci.* **2006**, *21*, 628–631.
3. Hayakawa, M.; Molchanov, O.A.; Ondoh, T.; Kawai, E. The precursory signature effect of the Kobe earth quake on VLF subionospheric signals. *J. Res. Lab. Tokyo* **1996**, *43*, 169–180.
4. Wang, J.; Chen, E.; Zhao, X. Observation and study on phase of very low frequency propagation over polar area. *Chin. J. Radio Sci.* **2006**, *21*, 385–390.
5. *DARPA-BAA-16-23*; Spatial, Temporal, and Orientation Information in Contested Environments (STOIC) Very Low Frequency (VLF) Positioning System. Strategic Technology Office: Arlington, VA, USA, 2016; pp. 2–24.
6. Budden, K.G. *Radio Waves in the Ionosphere*; Cambridge University Press: Cambridge, UK, 1961; p. 542.
7. Richardson, D.K.; Cohen, M.B. Seasonal variation of the D-region ionosphere: Very low frequency (VLF) and machine learning models. *J. Geophys. Res. Space Phys.* **2021**, *126*, e2021JA029689. [CrossRef]
8. Cohen, M.B.; Gross, N.C.; Higginson-Rollins, M.A.; Marshall, R.A.; Gołkowski, M.; Liles, W.; Rodriguez, D.; Rock Way, J. The lower ionospheric VLF/LF response to the 2017 Great American Solar Eclipse observed across the continent. *Geophys. Res. Lett.* **2018**, *45*, 3348–3355. [CrossRef]
9. Helliwell, R.A. *Whistlers and Related Ionospheric Phenomena*; Stanford University Press: Stanford, CA, USA, 1965.
10. Inan, U.; Chang, H.; Helliwell, R. Electron precipitation zones around major ground-based VLF signal sources. *J. Geophys. Res.* **1984**, *89*, 2891–2906. [CrossRef]
11. Abel, B.; Thorne, R.M. Electron scattering loss in Earth's inner magnetosphere: 1.Domin ant physical processes. *J. Geophys. Res. Space Phys.* **2012**, *103*, 2385–2396. [CrossRef]
12. Yang, M.; Peng, H.; Zheng, K.; Wei, G. Spatial Radiation Field Distribution of Underwater VLF Two-Element Antenna Array. *IEEE Trans. Antennas Propag.* **2023**, *71*, 1164–1169. [CrossRef]
13. Hayakawa, M. Whistlers. In *Handbook of Atmospheric Electrodynamics*; Volland, H., Ed.; CRC Press: Boca Raton, FL, USA, 1995; Volume 2, pp. 155–193.
14. Bortnik, J.; Inan, S. Precipitation of Radiation Belt Electrons by Lightning-Generated Magneto spherically Reflecting Whistler Waves. Ph.D. Thesis, Standford University, Standford, CA, USA, 2004.
15. Budden, K.G. *The Propagation of Radio Waves-the Theory of Radio Waves of Low Power in the Ionosphere and Magnetosphere*; Cambridge University Press: Cambridge, UK, 1988.
16. Zhao, S.; Liao, L.; Zhang, X.; Shen, X. Full wave calculation of ground-based VLF radiation penetrating into the ionosphere. *Chin. J. Radio Sci.* **2016**, *31*, 825–833.
17. Lehtinen, N.G.; Inan, U.S. Full-wave modeling of trans ionospheric propagation of VLF waves. *Geophys. Res. Lett.* **2009**, *36*, L03104. [CrossRef]
18. Pan, W.Y.; Li, K. *Propagation of SLF/ELF Electromagnetic Waves*; Springer Press: Berlin, Germany, 2014.
19. Samanes, J.; Raulin, J.; Jinbin, C. Estimation of the night time height of the lower ionosphere using VLF waves propagation. In Proceedings of the URSI Asia-Pacific Radio Science Conference, Seoul, Republic of Korea, 21–25 August 2016; pp. 1310–1312.
20. Zhang, S.X.; Wang, Y.S.; Li, G.M. Study on the influence of ionospheric parameters on the numerical calculation of VLF signal field strength. *Ship Electron. Eng.* **2018**, *38*, 140–144. (In Chinese)
21. He, T.; Zheng, J.; Pan, W.Y.; Li, K. Multiple-mode interference and phase standard deviation of VLF wave propagation in an anisotropic Earth–Ionosphere waveguide. *IEEE Trans. Antennas Propag.* **2018**, *66*, 7265–7272. [CrossRef]
22. Chowdhury, S.; Kundu, S.; Basak, T.; Ghosh, S.; Hayakawa, M.; Chakraborty, S.; Chakrabarti, S.K.; Sasmal, S. Numerical simulation on flower ionospheric reflection parameters by using international reference ionosphere (IRI) model and validation with Very Low Frequency (VLF) radio signal characteristics. *Adv. Space Res.* **2021**, *67*, 1599–1611. [CrossRef]
23. Liu, B.; Wang, M.; Zhang, S.; Li, H.; Li, G.; Yu, M.; Zhang, X.; Xu, J. Finite Element Method study on VLF propagable modes coupling and interference in the anisotropic earth-ionosphere waveguide. *Int. J. Numer. Model. Electron. Netw. Devices Fields* **2024**, *37*, e3207. [CrossRef]
24. Wait, J.R. *Electromagnetic Waves in Stratified Media*; Pergamon Press: New York, NY, USA, 1962; p. 609.
25. Fu, H.; Zhang, Z.; Ju, J. Calculation of short wave propagation in anisotropic ionosphere by transfer matrix Method. In Proceedings of the Electronic and Automation Control Conference (IAEAC), Chengdu, China, 12–14 March 2021; p. 5.
26. Liu, R.; Xu, Z.; Wu, J.; Liu, S.; Zhang, B.; Wang, G. Preliminary studies on ionospheric for easting in China and its surrounding area. *J. Atmos. Sol.-Terr. Phys.* **2005**, *67*, 1129–1136. [CrossRef]
27. Berreman, D.W. Optics in stratified and anisotropic media: 4×4 matrix formulation. *J. Opt. Soc. Am. B* **1972**, *62*, 503. [CrossRef]
28. Zhao, L.; Xie, H. A novel optical ε-near-zero material realized by multi-layered Ag/SiC filmstructures. *Optik* **2019**, *183*, 519. [CrossRef]